minerals

MDPI

Article

Exploring Lower Cretaceous Karst Bauxite from South-Central Pyrenean Unit (NE Spain): Genesis and Ceramic Potential

Alfonso Yuste [1,*], Blanca Bauluz [1] and Elisa Laita [2]

[1] Instituto Universitario de Ciencias Ambientales de Aragón-Universidad de Zaragoza, Campus San Francisco, 50009 Zaragoza, Spain; bauluz@unizar.es
[2] CNRS, Institut des Sciences Analytiques et de Physico-Chimie pour l'Environnement et les Matériaux (IPREM), Université de Pau et des Pays de l'Adour, UMR 5254, 64000 Pau, France; elisa.laita-florian@univ-pau.fr
* Correspondence: alfon@unizar.es

Abstract

This study investigates a karst bauxite deposit from NE Spain with a dual objective incorporating the novel aspect of directly linking genetic processes to industrial ceramic performance. First, the bauxite is mineralogically and texturally characterized using X-ray diffraction and field emission scanning electron microscopy. Second, the mineralogical and textural transformations of the bauxite during firing at 1000, 1200 and 1300 °C are analyzed, together with their effects on the physical properties of the fired products. The Lower Cretaceous bauxite is autochthonous, shows a pisolithic structure, and formed in situ under tropical monsoon conditions through intense chemical weathering involving dissolution–crystallization processes. For ceramic testing, the bauxite was mixed with illitic–kaolinitic clays in a 90/10 proportion. During firing, kaolinite and illite destabilize and transform into mullite, initially by solid-state reactions at 1000 °C and subsequently by crystallization from a vitreous phase at higher temperatures, producing larger crystals and composition closer to the empirical mullite formula. The formation of vitreous phase and mullite leads to reduced porosity and increased density and linear shrinkage, particularly between 1000 and 1200 °C. Specimens fired at 1300 °C show higher mechanical strength, related to higher mullite content and a larger size of its crystals. The results demonstrate the potential interest of these bauxites for ceramic manufacturing.

Keywords: karst bauxite; palaeoclimate; Lower Cretaceous; kaolinite; ceramics; FESEM

1. Introduction

The analysis of bauxites is of great interest due to their geological and industrial implications. Bauxites are paleosols formed through intense chemical weathering under hot and humid tropical conditions, making them excellent climate proxies; therefore, their mineralogical characterization has been widely used for paleoclimatic reconstructions [1–5]. Nevertheless, several important issues must be considered when using these materials to infer climatic conditions, such as the autochtonous or allochtonous nature of the deposits, among others. Likewise, during bauxite formation, the superposition of different mineral genesis processes is common [4], giving rise to complex textural relationships among the different phases. For this reason, it is crucial to carry out detailed microtextural studies mainly by means of electron microscopy, due to the fine size of the constituent minerals, frequently smaller than 1 μm, in order to elucidate the precise conditions that led to the formation of these materials.

Received: 17 January 2026
Revised: 2 February 2026
Accepted: 5 February 2026
Published: 6 February 2026

The common micron-sized constituent minerals of bauxites include, in addition to Al hydroxides and oxyhydroxides (such as gibbsite, boehmite and diaspore), Fe oxides and oxyhydroxides (e.g., hematite and goethite) and, frequently, high contents of kaolinite, e.g., [6–9]. In fact, from an industrial point of view, bauxites are currently being investigated as a source of kaolin [10]. Nowadays, demand for and applications of kaolin are increasing significantly, although its availability is decreasing [11]. Among others, an important traditional application of kaolinite-rich materials is the ceramic industry. With regard to bauxites, due to their Al content, mainly as Al hydroxides and oxyhydroxides, they can constitute important raw materials for the manufacture of refractory ceramics e.g., [12–15]. Also, they have been proven to be an inexpensive substitute for alumina in mullite production [16]. Although millions of metric tons of bauxites are available worldwide, their use is mainly limited to Al extraction [17].

The mineralogical composition and textural features of bauxites when used as raw materials for ceramic industry, as well as the firing temperature and the kiln atmosphere, determine the mineral transformations that occur during high temperatures firing [15,18]. Furthermore, the physical properties of the ceramic products are controlled by these mineral transformations during firing. Research focused on the detailed mineral and textural transformations that take place during firing of bauxite materials is scarce. Therefore, expanding our knowledge in this field and exploring its relationship with the physical properties of the final product is essential for evaluating its potential as a raw material for the ceramic industry.

In this research, a karst bauxite deposit located in the Central South Pyrenean Unit (NE Spain), was investigated with a dual purpose. Accordingly, the objectives of this work are: (1) to comprehensively characterize the bauxite deposit mineralogically and texturally in order to establish its genesis and integrate the findings within regional geological and global paleoclimatic contexts; and (2) to investigate the mineralogical and textural transformations of this bauxite material during firing at different temperatures, and to assess how these changes influence the physical properties of the resulting ceramic products, thereby evaluating its potential for ceramic production.

To achieve the first objective, the material was characterized from a mineralogical and textural point of view using X-ray diffraction and field emission scanning electron microscopy (FESEM). This characterization not only allows the formation conditions of the deposit to be elucidated and the data to be integrated into local and regional geological frameworks and global paleoclimatic models, but is also essential for understanding the mineralogical and textural transformations occurring during ceramic processing.

To achieve the second objective, the bauxite material was mixed with illitic-kaolinitic clays in a 90/10 proportion (to facilitate specimen preparation) and fired at 1000, 1200 and 1300 °C. Consequently, this approach allows the relationships between mineralogical transformations, starting material characteristics, and the physical properties of the fired products to be determined.

2. Materials Under Study

Karst bauxites are those bauxite deposits that overlie carbonate rocks [1]. According to this author, an important number of karst bauxites are Mediterranean-type, and they commonly show karstified bedrock surfaces. There are three important areas in NE Spain where this type of karst bauxites occurs: the South Pyrenean Zone, the Catalonian Coastal Range, and the Maestrazgo Basin. This paper deals with one deposit located in the South Pyrenean Zone.

Geologically, the deposit is located in the Sierras Marginales of the Central South Pyrenean Unit, where significant bauxite outcrops are present. Specifically, the materials

under study come from an outcrop in an old quarry located on the SW slope of the Sant Mamet Dome, NW of the Alós de Balaguer locality (Lérida, NE Spain) (N41°57′21.7″; E0°57′10.7″) (Figure 1).

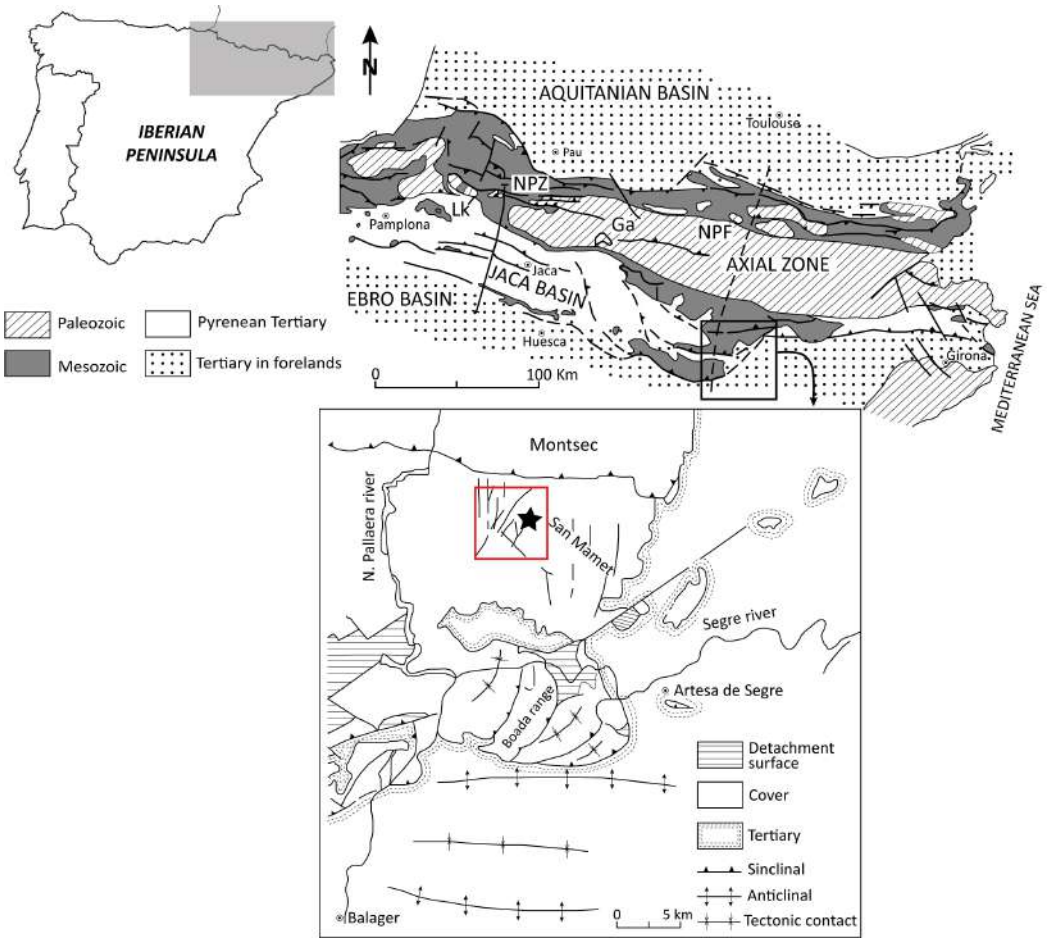

Figure 1. Geological sketch and location of the study area (red square) and the outcrop (black star). Modified from [19,20].

In the study area, a mid-Jurassic (Dogger) stretch of coarse-grained, massive dolomite is observed, characterized by high porosity and the presence of numerous cavities [21,22]. The original facies cannot be recognized due to intense dolomitization, and the upper surface shows important karst development. The bauxite deposit is located at the base of the Cretaceous materials, which unconformably overlie the Jurassic dolomites, within cavities produced by the paleokarst processes. The bauxite unit may contain intercalations of sand and quartz gravel [21]. Its thickness is variable depending on the irregularities of the bedrock surface and is Aptian–Santonian in age [22,23].

Overlying the bauxite deposit, there is a dm- to cm-thick level of Santonian sandstones and gravels exhibiting cross-lamination and bioturbation [21,23].

The study outcrop constitutes a bauxite deposit approximately 6 m thick (Figure 2), although the current conditions of the outcrop do not allow the morphology of the deposit to be accurately appreciated, due to past mining activity. Metric blocks of Jurassic dolostone with a whitish-yellowish color can be observed at the base of the outcrop. To the top, yellowish Santonian sandstones are visible. Above the dolostone level, the predominantly red bauxite is found (Figure 2). Nevertheless, a whitish level can be observed in the middle of the deposit and more purplish colors are appreciated towards the top. To the naked eye, the most striking feature of the bauxite is its pisolithic character (Figure 2). It consists of

abundant pisoliths most frequently spherical in shape and rounded edges, with an average diameter of 2–3 mm and up to 7–8 mm.

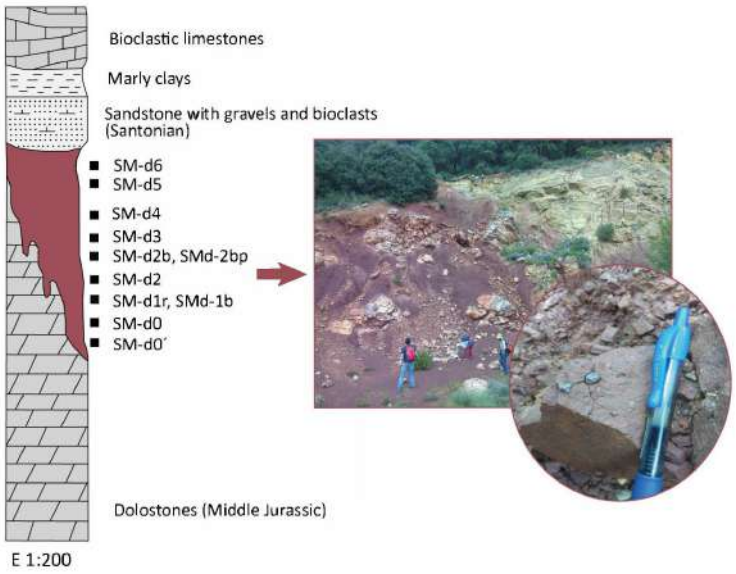

Figure 2. Location of samples in the study profile and field view of the predominantly red bauxite constituting the study outcrop. The pisolithic texture is observable to the naked eye.

As commented before, the bauxite material was mixed with illitic-kaolinitic clays in a 90/10 proportion (90% bauxite, 10% illitic-kaolinitic clay). This minor clay addition was used solely to enhance plasticity and facilitate specimen preparation, and it is not expected to significantly affect the properties of the fired materials. In agreement with this assumption, [15] showed that even higher clay contents (25 wt%) in bauxite–clay mixtures enable the development of refractory properties at reduced firing temperatures. These clays belong to the Albian Escucha Fm and come from the vicinity of the locality of Ariño (Teruel, NE Spain).

3. Methodology

3.1. Mineralogical and Chemical Characterization

A representative sampling of the deposit was carried out with the objective of its mineralogical and textural characterization. A total of 9 samples were taken, whose location is shown in Figure 2. The sample SMd-1 was subdivided into two subsamples, a reddish and a whitish one (SMd-1r and SMd-1b, respectively). Also, pisoliths included in sample SMd-2b were separated to be analyzed by X-ray diffraction (subsample SMd-2bp). For the manufacture of the specimens to be fired at different temperatures, 3 kg of the predominantly red bauxite from the lowermost part of the outcrop were taken, where the X-ray diffraction study evidenced the highest boehmite contents.

The whole-rock mineralogical composition of the samples, including the fired products at different temperatures and the <2 μm fraction mineralogical composition of the bauxite samples, were determined by X-ray diffraction (XRD) by means of a Philips PW 1710 diffractometer (Philips, Amsterdam, The Netherlands), with Cu-Kα radiation, automatic divergence slit, and a graphite monochromator. XRD patterns were obtained from the 3–80 and the 3–30 °2θ intervals, for the whole rock and the <2 μm fraction, respectively. The <2 μm fraction was concentrated by centrifuge and analyzed in air-dried oriented aggregates. To store the XRD data, the XPowder (v2017) software by [24] was used. Abundances of whole-rock mineral phases were determined using the reference intensity ratios (RIRs) given by [25]. For the semi-quantification of phyllosilicate abundances in the <2 μm frac-

tion, the RIR values of [26] were used. It should be noted that RIR-based semiquantitative XRD analysis is subject to significant uncertainties, particularly due to limited accuracy and the inability to quantify amorphous and very fine-grained phases. Therefore, the results are used only for relative comparison between samples rather than for absolute quantitative interpretation. Kaolinite crystallinity (KC) was calculated measuring the full width at half maximum (FWHM) of the 7Å reflection in the air-dried oriented aggregates.

Both transmitted and reflected light optical microscopy were used to examinate the samples in a first approach. For the description of the pisolithic texture of the bauxite, the terms given by [1] were considered: macropisoids (>5 mm), pisoids (5–1 mm), ooids (1000–100 μm) and micro-ooids (<100 μm). For a more precise textural characterization and to obtain chemical information of the mineral phases, selected samples were observed by field emission scanning electron microscopy (FESEM) using secondary electron (SE), backscattered electron (AsB), energy-dispersive backscattered electron (ESB), and energy-dispersive X-ray (EDS) detectors. The study was carried out using a Carl Zeiss MERLIN FESEM (Carl Zeiss Microscopy GmbH, Jena, Germany) equipped with an Oxford instrument detector (EDS) (Oxford Instruments, High Wycombe, UK). SE images were acquired with an accelerating voltage of 15 kV and a beam current of 600 pA. The accelerating voltage for the acquisition of the AsB images and the EDS semiquantitative analyses (with a detection limit of 0.1%) was 15 kV with a beam current of 600 pA, and a counting time of 50 s for analysis; for the EsB images, the accelerating voltage was 4 kV with a beam current of 1 nA. Samples were carbon coated prior to the FESEM study.

3.2. Physical Properties of the Fired Products

For the manufacture of the specimens to be fired, the bauxite and the illitic-kaolinitic clay were milled under 100 μm. The mixture of the bauxite and the illitic-kaolinitic clay, in a 90/10 proportion, was used to produce cylinders of 5 cm in diameter and 0.8 cm high by pressing. These cylinders were fired in a Tecno-piro PR4T oven at 1000 °C, 1200 °C and 1300 °C under oxidizing conditions. Increasing temperature was achieved in steps of 200 °C/h and the maximum temperature was maintained for 2 h. Cylinders made from the raw and the fired samples are shown in Figure 3.

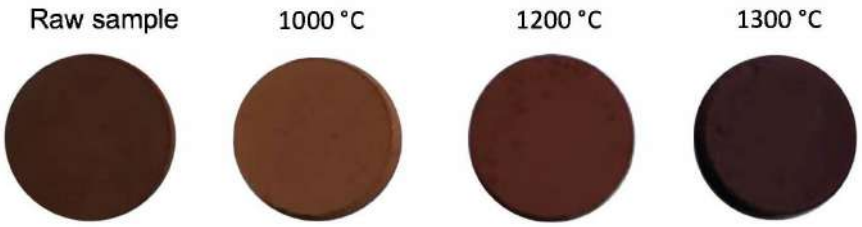

Figure 3. Raw and fired cylinders obtained from the mixture of the bauxite (90%) with the kaolinitc clay (10%).

The specimens, both raw and fired at the different temperatures, were measured and weighed to determine density and weight loss. To determine the linear shrinkage of the fired samples the following formula was applied:

$$LS(\%) = (D1 - D2/D1) \times 100$$

where D1 is the diameter of the raw sample and D2 is the diameter of the fired sample.

An X·Rite portable spectrophotometer, model Ci6X, was used for the determination of the precise color of the fired samples, which yields color values in the Munsell system and in the CIE L*a*b* scale. It was used to measure color values in both the raw and fired samples.

Porosimetric analyses were carried out by means of An Ultrapyc 1200e Helium Pycnometer (Quantachrome Instruments, Boynton Beach, FL, USA) in the Thermal Analysis and Porous Solids Unit of the University of Alicante (Spain). They provided, for the fired samples, the pore size and distribution, as well as their total porosity.

Finally, point load test (PLT) was carried out on the fired samples. This permitted the calculation of the point load resistance index $I_{s(50)}$. Although the point load test is traditionally used in rock mechanics, it has also been applied to fired bauxite–clay ceramic materials and successfully compared with commercial bauxites [15], supporting its suitability for comparative mechanical assessment in this study. To achieve the data, a point load measuring equipment was used to obtain the point load value of each sample (I_s) in kg/cm^2. Between 10 and 12 measurements were carried out per sample. Measurements were achieved from prisms (approximately 7 × 7 × 10 mm) obtained from the original cylinders fired at the quoted temperatures. The prisms were obtained by cutting the fired cylindrical samples along their diameter (5 cm). In this way, prismatic specimens with a height of 10 mm were prepared from the lateral dimension of the cylinders. A correction factor was necessary to obtain the $I_{s(50)}$ index, according to the expression:

$$I_{s(50)} = F \cdot I_s$$

where F is the correction factor that was obtained using the formula:

$$F = (D_e/50)^{0.45}$$

D_e being the equivalent diameter of the regular prisms, which is calculated according to the following:

$$D_e^2 = 4A/\pi$$

where A is the minimum cross-sectional area that contains the two load application points.

4. Results

4.1. Mineralogical Composition of the Bauxite and the Fired Products

Table 1 and Figure 4 show the mineralogical compositions of the studied samples. The main phases are kaolinite (20%–48%), boehmite (7%–47%; absent in one sample, the one with the highest kaolinite content) and hematite (16%–38%). Goethite, anatase, rutile, gibbsite, quartz, calcite and diaspore have been identified as accessory phases.

At the base of the profile, kaolinite and boehmite predominate, whereas hematite is less abundant (Figure 4). To the top, the kaolinite content remains constant with variable amounts of boehmite and hematite, except for the sample where boehmite is absent. The above quoted reddish subsample SMd-1r exhibits a higher concentration of hematite (26%) than the whitish one Smd-1b (18%), but the latter shows a higher concentration of boehmite (47% vs. 22%), both presenting a similar kaolinite content (26%–27%). Regarding the pisoliths from sample Smd-2b (subsample Smd-2bp), they show similar kaolinite (26%) and hematite (28%) contents to the sample where they are included, but the boehmite content is much lower (7%) and the goethite content is higher.

Regarding the <2 μm fraction, all samples are constituted exclusively by kaolinite. Kaolinite crystallinity (FWHM) is very similar throughout the entire profile (0.2 to 0.4), being somewhat higher to the top of the profile (Figure 4).

Table 1. Mineralogical composition (%) of the study samples. Kln: kaolinite, Bhm: boehmite, Hem: hematite, Gt: goethite, Ant: anatase, Rt: rutile, Gbs: gibbsite, Qtz: quartz, Cal: calcite, Dsp: diaspore, tr: traces.

	Whole Sample									
Sample	**Kln**	**Bhm**	**Hem**	**Gt**	**Ant**	**Rt**	**Gbs**	**Qtz**	**Cal**	**Dsp**
SMd-0	35	40	17	6	tr	tr	-	-	-	-
SMd-0′	35	40	16	5	tr	tr	-	-	-	-
SMd-1r	26	22	26	-	tr	tr	7	-	tr	10
SMd-1w	27	47	18	-	tr	tr	-	-	-	-
SMd-2	22	36	34	-	tr	5	-	-	-	-
SMd-2b	32	22	26	10	-	-	7	-	tr	-
SMd-2bp	26	7	28	25	-	tr	-	11	-	-
SMd-3	25	23	38	6	tr	-	-	-	tr	-
SMd-4	22	38	34	-	tr	tr	-	-	-	-
SMd-5	46	-	30	-	tr	tr	8	tr	5	-
SMd-6	20	38	35	-	tr	-	-	tr		-

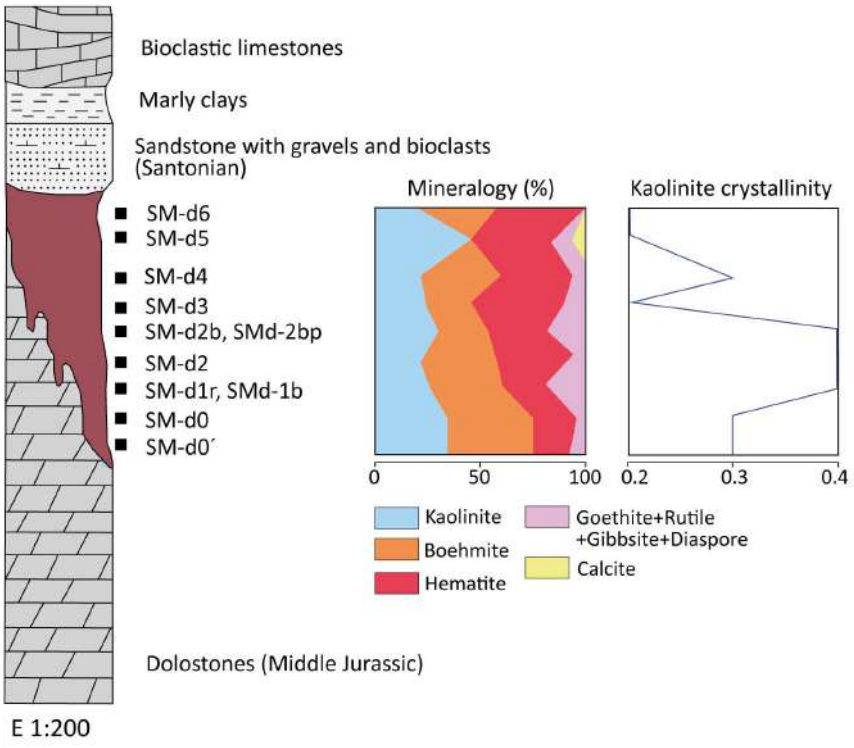

Figure 4. Mineralogical composition (%) and kaolinite crystallinity of the studied samples.

On the other hand, the bauxite sample used as raw material for the specimens to be fired at different temperatures contains 39% kaolinite, 37% boehmite, and 12% hematite, with goethite, anatase, and rutile as accessory phases. The illitic-kaolinitic clay from the Escucha Fm with which the bauxite was mixed is made up of 33% illite, 20% kaolinite and 42% quartz, with albite and orthoclase as accessories. The mixture used for the manufacture of the specimens to be fired shows a mineralogical composition very similar to that of the bauxite (Table 2). XRD patterns of the bauxite, the illitic-kaolinitic clay and the 90/10 mixture are shown in Figure 5.

Table 2. Mineralogical composition (%) of the raw materials and the fired products. Bhm: boehmite, Kln: kaolinite, Ill: illite, Mc: mica, Hem: hematite, Gt: goethite, Ant: anatase, Rt: rutile, Qtz: quartz, Ilm: ilmenite, Crist: cristobalite, Cor: corundum, Mu: mullite, Ab: albite, Orth: orthoclase, tr: traces.

	Bauxite (BX)	Illitic-Kaolinitic Clay (KC)	BX90/KC10	1000 °C	1200 °C	1300 °C
Bhm	37	-	35	-	-	-
Kln	39	20	34	-	-	-
Ill/Mc	6	33	11	-	-	-
Hem	12	-	9	23	11	8
Gt	tr	-	tr	-	-	-
Ant	tr	-	tr	tr	-	-
Rt	tr	-	tr	tr	tr	tr
Qtz	-	42	5	15	tr	tr
Ilm	-	-	-	6	-	-
Crist	-	-	-	tr	tr	tr
Cor	-	-	-	11	tr	tr
Mu	-	-	-	33	83	86
Ab	-	tr	-	-	-	-
Orth	-	tr	-	-	-	-
γ-alumina	-	-	-	tr	-	-

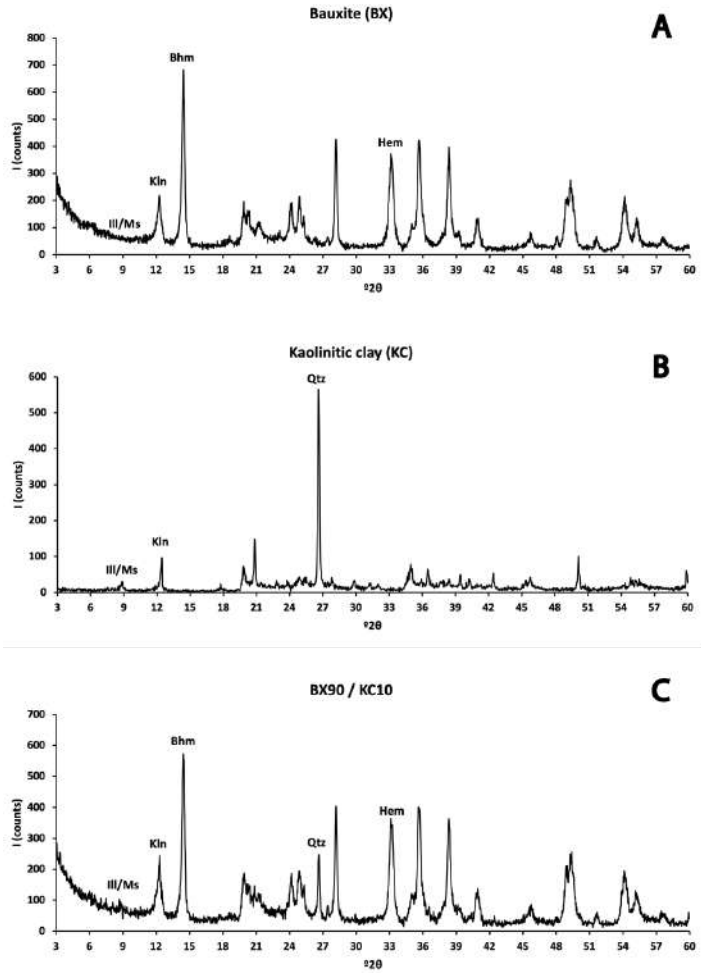

Figure 5. XRD patterns of the raw materials used for the manufacture of the ceramic specimens. (**A**) Bauxite; (**B**) illitic-kaolinitic clay; (**C**) mixture of bauxite (90%) and illitic-kaolinitic clay (10%). The most representative diffraction peaks of the minerals present are labeled. Ill/Ms: illite/muscovite phases; Kln: kaolinite; Bhm: boehmite; Hem: hematite; Qtz: quartz.

Table 2 also shows the mineralogical composition of the fired samples at different temperatures, reflecting the mineral transformations that take place during firing.

At 1000 °C the main mineral phases are mullite, hematite, quartz and corundum, accompanied by ilmenite and, to a lesser extent, anatase, rutile and cristobalite. The XRD pattern run between 35 and 70 °2θ revealed the presence of γ-alumina, with its characteristic reflection peak at 67 °2θ. This phase was not semiquantified since there was no RIR value available. At 1200 °C there is a decrease in the content of all mineral phases except for mullite, which exhibits a notable increase. Along with mullite, hematite is detected in a lower proportion than in the sample fired at 1000 °C, and corundum, quartz, cristobalite and rutile occur as accessory phases. Finally, the sample fired at 1300 °C has a composition similar to the previous one, with mullite as the most abundant mineral, accompanied by hematite along with traces of corundum, quartz, cristobalite and rutile.

4.2. Textural Characterization of the Bauxite and the Fired Products

As mentioned, the bauxite exhibits a pisolithic texture, characterized by the presence of abundant pisoliths embedded in a clay matrix. In general, they contain higher amounts of Fe oxides than the matrix.

FESEM images (Figure 6) show that kaolinite and Al hydroxides (mainly boehmite, in agreement to XRD results), randomly arranged, are the main phases constituting the matrix of the samples, along with Fe oxides and, to a lesser extent, Ti oxides. Kaolinite occurs as nanometric, idiomorphic to subiomorphic platy crystals often with a hexagonal outline (Figure 6A). It also occurs as lamellar aggregates up to 2 μm in diameter and book-type aggregates up to 3.5 μm thick approximately (Figure 6B). Boehmite is observed as tiny, nanometric idiomorphic to subidiomorphic crystals, with a prismatic and planar habit. It occurs finely mixed with kaolinite or cementing it (Figure 6C). Also, it has been observed between the layers of book-type kaolinite aggregates (Figure 6D). Both kaolinite and Al hydroxides have also been observed filling cavities (Figure 6E). Finely disseminated between kaolinite and boehmite, nanometer-sized Fe oxides (mainly hematite) are common (Figure 6B,C,E). They usually occur as rounded crystals of irregular outlines or exhibit elongated, laminar habit (Figure 6F). Sometimes they have been observed between the layers of kaolinite aggregates.

With regard to the pisoliths, their morphology is fundamentally spheroidal, and less frequently irregular or elongated. In the studied samples ooids, pisoids and micro-ooids predominate, in this order, whereas macropisoids are observed very occasionally.

BSE images show that, in general, micro-ooids and ooids are massive, exhibiting a clayey texture similar to that of the matrix, although some detrital particles randomly arranged can be recognized (Figure 7A). Some of the larger ooids can exhibit a core surrounded by several concentric layers (Figure 7A). In these cases, the core can consist of an irregular particle or be massive, and include small irregular particles and fragments of micro-ooids. Externally, they all frequently present an Fe oxides-rich cortex.

On the contrary, pisoids and macropisoids are commonly formed by a core surrounded by several concentric layers (Figure 7A) although occasional massive ones can be observed. The core is frequently massive, with a clayey texture, and can include smaller ooids and detrital particles (Figure 7A–D). Fe oxides, as crystals of elongated sections, are very abundant along with irregular, elongated Al hydroxides and kaolinite, as platy crystals or laminar aggregates (Figure 7B) and as book-type aggregates. Fe oxide crystals are commonly observed between the kaolinite layers of book-type aggregates (Figure 7C). The concentric layers surrounding the core are determined by the different proportions of Fe oxides, Al hydroxides and kaolinite (Figure 7E). Texturally, these phases are similar to those observed in the matrix of the bauxites. In some cases, the concentric layers can encompass

and adapt to particles or accumulations of certain mineral phases, such as Al hydroxides or Fe oxides (Figure 7F). As for ooids and micro-ooids, a ferruginized external cortex is common in pisoids and macropisoids (Figure 7A,D).

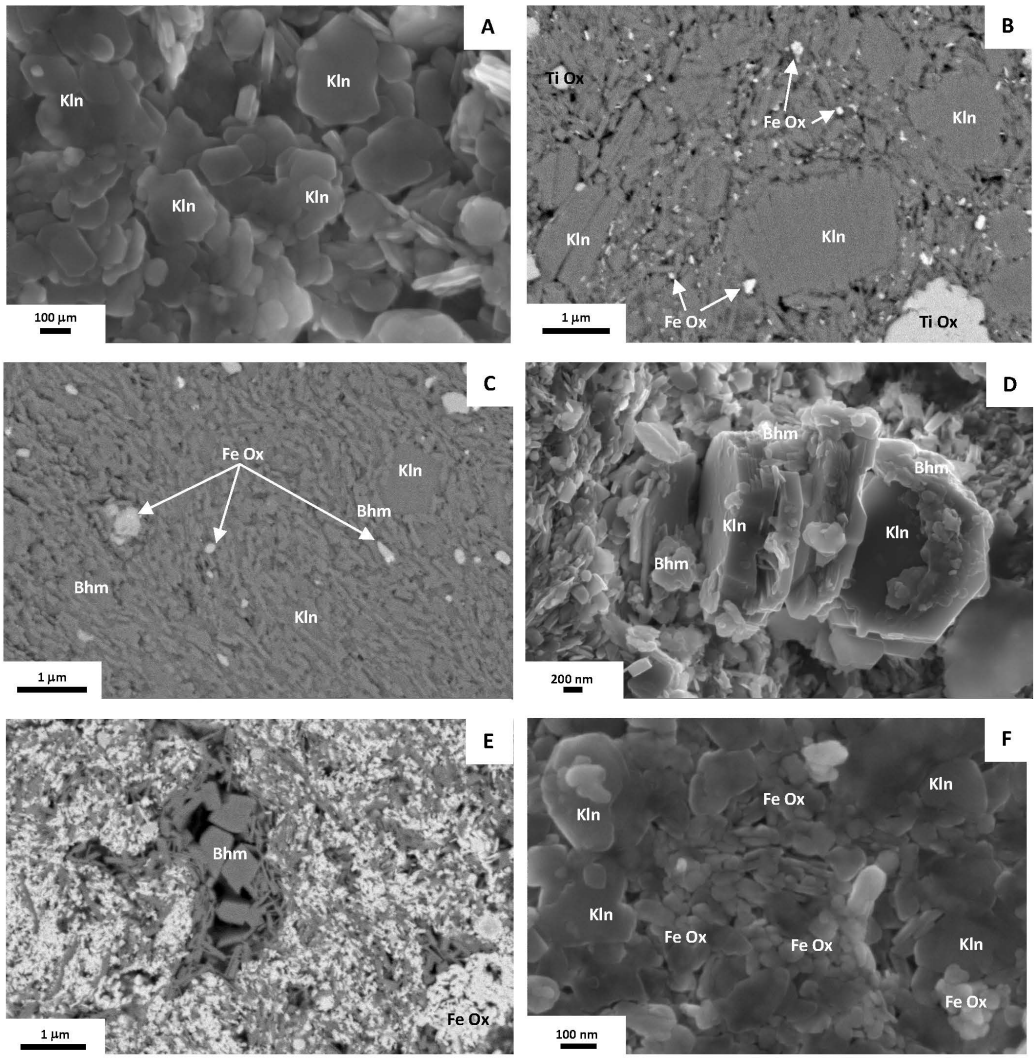

Figure 6. Representative FESEM images of the matrix of the studied bauxite. (**A**) Nanometer-sized, idiomorphic to subidiomorphic kaolinite with common hexagonal outlines. (**B**) Platy kaolinite and book-type aggregates of kaolinite; nanometric Fe oxides are finely dispersed throughout the matrix and Ti oxides are also observable. (**C**) Elongated boehmite crystals cementing kaolinite. (**D**) Boehmite between the layers of a book-type aggregate of kaolinite and cementing it. (**E**) Idiomorphic to subidiomorphic boehmite filling cavities. (**F**) Subidiomorphic kaolinite and nanometer-sized Fe oxides of irregular or rounded outlines and laminar habit. Kln: kaolinite; Bhm: boehmite; Fe Ox: Fe oxides; Ti Ox: Ti oxides.

Furthermore, irregular fragments of pisoliths can be observed (Figure 7G), as well as radially or randomly arranged fractures affecting the pisoliths (Figure 7E). These fractures do not usually affect the ferruginized cortex commonly observed and are filled by the same phases observed in the matrix of the bauxites, such as book-type aggregates of kaolinite and Fe oxides (Figure 7H).

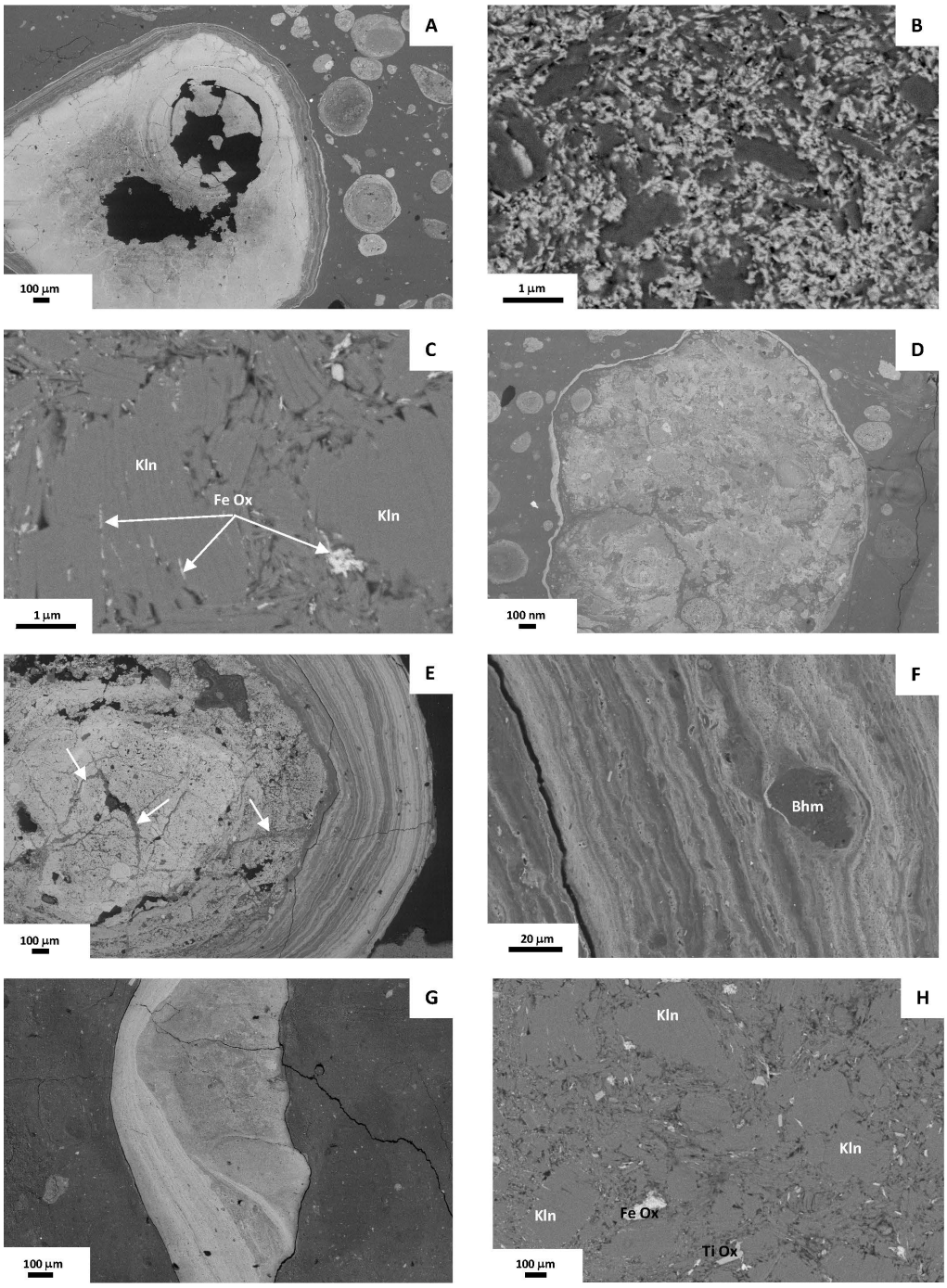

Figure 7. Representative FESEM images of different aspects with regard to pisoliths of the study bauxite. (**A**) Ooids and micro-ooids and a pisoid including an ooid in the core. (**B**) Elongated crystal of Fe oxides and platy crystals and laminar aggregates of kaolinite in the core of a pisoid. (**C**) Fe oxides between the kaolinite layers of book-type aggregates. (**D**) Pisoid with a large core including ooids and detrital particles and surrounded by an Fe-rich cortex. (**E**) Pisoid whose core is affected by radial or randomly arranged fractures (white arrows); the concentric layers surrounding the core are determined by the different proportion of Fe oxides, Al hydroxides and kaolinite. (**F**) Accumulation of boehmite encompassed by the concentric layers, which adapt to it. (**G**) Fragment of a pisoid. (**H**) Book-type aggregates of kaolinite and Fe oxides filling fractures affecting pisoids. Kln: kaolinite; Bhm: boehmite; Fe Ox: Fe oxides; Ti Ox: Ti oxides.

With regard to transformations taking place during firing, textural transformations at 1000 °C are relatively scarce, with no strong signs of fusion. Rounded fragments of

the original rocks, both the bauxite and the illitic-kaolinitic clay, can be still observed (Figure 8A). In the bauxite fragments, typical morphologies of phyllosilicates, mainly kaolinite, the most abundant in the raw material, can be observed, including book-type aggregate morphologies (Figure 8B). EDS analyses carried out on these phases indicate mullite-type compositions with the average structural formula of $Al_{3.3}Si_{2.2}Fe_{0.4}O_{9.8}$. In some analyses, an Al excess has been obtained compared with the empirical formula of mullite ($Al_{4.5}Si_{1.5}O_{9.8}$), which may be due to the presence of small-sized corundum and γ-alumina, as indicated by the XRD results. Fe in the analyses may be due either to the presence of nanometric Fe phases (oxides) or to the presence of Fe in the mullite structure, given the abundance of Fe oxides in the raw material. In addition to Fe oxides, Ti oxides (rutile or anatase) have been identified, which in some cases show compositional zoning with ilmenite (Figure 8C). On the other hand, in the illitic-kaolinitic clay fragments, anhedral clasts of quartz are observed along with phases showing lamellar morphologies, corresponding to the abundant original illite, although they exhibit mullite composition (Figure 8D).

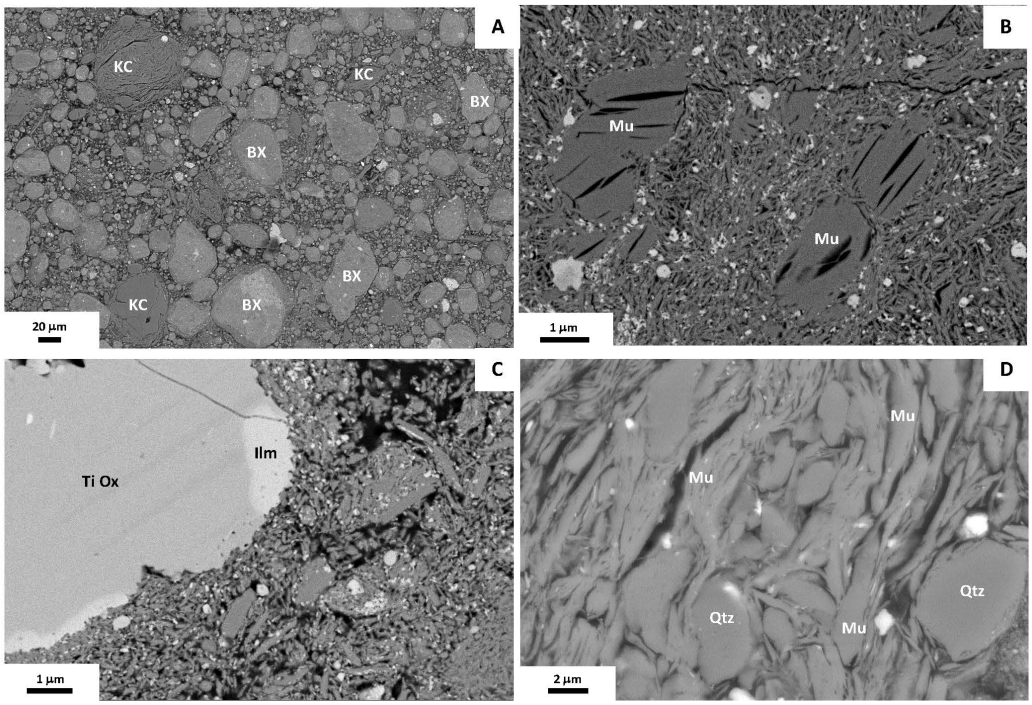

Figure 8. Representative FESEM images of the sample fired at 1000 °C. (**A**) Fragments of the original rocks can be still recognized, both the bauxite (BX) and the illitic-kaolinitic clay (KC). (**B**) Typical morphologies of kaolinite with mullite composition. (**C**) Compositional zoning involving Ti oxide and ilmenite in a crystal from a bauxite fragment. (**D**) Anhedral clasts of quartz and lamellar phases, corresponding to the abundant original illite from the illitic-kaolinitic clay, exhibiting mullite composition. Mu: mullite, Ti Ox: Ti oxides, Ilm: ilmenite, Qtz: quartz.

In the sample fired at 1200 °C, greater textural homogeneity is observed. The rock fragments can still be identified but they show more diffuse edges and signs of fusion and recrystallization are evident (Figure 9A). Quartz grains with diffuse reaction edges are common. (Figure 9B). No phyllosilicate morphologies are observed anymore. The most striking feature is the presence of abundant nanometric acicular mullite crystals (up to 1 µm), immersed in a Si-rich homogeneous matrix with the appearance of a vitreous molten phase (Figure 9B,C). The average formula of mullite crystals ($Al_{3.8}Si_{1.8}Fe_{0.3}Ti_{0.1}O_{9.8}$) is closer to the empirical one. Nanometer-sized Fe- and Ti- oxides are also observable, mainly

disseminated in the molten matrix (Figure 9B,C) or inside the fragments that presumably corresponded to the original bauxite.

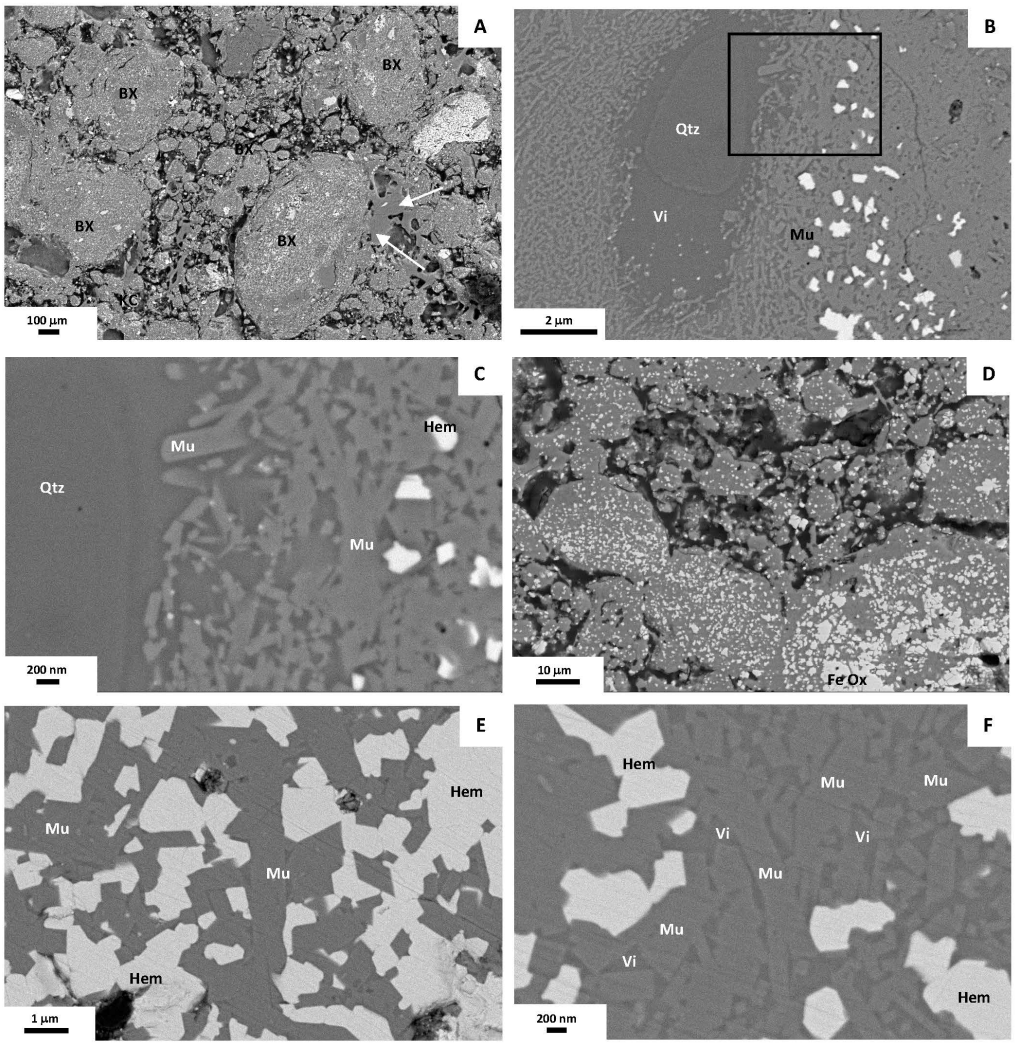

Figure 9. Representative FESEM images of the samples fired at 1200 °C (**A**–**C**) and 1300 °C (**D**–**F**). (**A**) Fragments of the original bauxite (BX) are observable with more diffuse boundaries than at 1000 °C; signs of fusion (white arrows) are evident too. (**B**) Quartz clasts show diffuse reaction edges and a vitreous phase (Vi) can be recognized; mullite crystals are disperse in the vitreous phase. (**C**) A detail of the black square in the previous microphotograph where prismatic to acicular mullite crystals can be observed. (**D**) Fragments of the original bauxite (BX) are observable with more diffuse boundaries than at 1200 °C. (**E**) Mullite crystals and hematite are the only observable phases at 1300 °C. (**F**) Mullite crystals and hematite are disperse in a vitreous phase. Mu: mullite, Qtz: quartz, Hem: hematite.

Finally, at 1300 °C observations reveal a more homogeneous texture than in the samples fired at lower temperatures, with more diffuse grain boundaries (Figure 9D). Only mullite and Fe oxides are mainly present (Figure 9E,F). Mullite shows a very similar composition to that calculated in the sample fired at 1200 °C ($Al_{3.8}Si_{1.9}Fe_{0.3}O_{9.8}$) and occurs as acicular, prismatic nanometer- to occasionally micrometer-sized crystals (Figure 9E,F). It is distributed relatively homogeneously along with neoformed Al-bearing hematite, which occurs disseminated or forming aggregates (Figure 9E,F) in the fragments presumably coming from the bauxite.

4.3. Physical Properties of the Fired Products

Density, linear shrinkage and weight loss values are shown in Table 3. The density of the raw sample has an average value of 1.85 g/cm^3. At 1000 °C the average density is 1.86 g/cm^3, whereas at 1200 °C and 1300 °C the average values are 2.46 g/cm^3 and 2.52 g/cm^3, respectively. Linear shrinkage increases from values close to 5% at 1000 °C to average values of 13.1% and 13.31% at 1200 °C and 1300 °C, respectively. Regarding weight loss, the values increase in the specimens fired at 1200 °C compared to those fired at 1000 °C, with a decrease observed in the specimens fired at 1300 °C.

Table 3. Density, linear shrinkage and weight loss of the study material.

	n	Density (g/cm^3)	Linear Shrinkage (%)	Weight Loss (g)
Raw	1	1.82		
	2	1.88		
1000 °C	1	1.87	4.75	3.49
	2	1.86	5.29	3.48
1200 °C	1	2.45	13.10	3.67
	2	2.47	13.13	3.70
1300 °C	1	2.53	13.57	3.52
	2	2.50	13.06	3.29

The color of the samples varies with the increase in temperature from dull reddish-brown in the raw specimen to bright reddish-brown at 1000 °C, red in the specimen fired at 1200 °C and dark reddish-brown at 1300 °C (Figure 10A). The results obtained in the CIE L*a*b* System are represented in Figure 10, which shows that firing at 1000 °C involves the projection of the color towards lighter and reddish tones than the raw sample. On the other hand, firing at 1200 °C darkens the color tone and projects it towards purple tones. Finally, firing at 1300 °C provokes the darkest tone and the color projection towards the bluest tones. It can be pointed out that the samples present a reddish-brown color at all firing temperatures and that the darkening does not increase linearly with the firing temperature.

Data obtained from the porosimetric analyses are shown in Figure 11, where pore radius, expressed in microns, and the percentage of intruded gas has been plotted. The maximum intrusion percentage of the sample fired at 1000 °C is 2.5% and corresponds to the pore radius between 1×10^{-1} and 1 µm. In addition, three minor peaks can be observed at this temperature: approximately 1% intruded in pores with radii between 1×10^{-2} and 1×10^{-1} µm; 0.5%–0.75% intruded in pores of radii in the range between 1×10^{-3} and 1×10^{-2} µm; and 0.25% intruded in pores with radii between 1×10^{2} and 1×10^{3} µm. At 1200 °C, the peak corresponding to pore radii between 1×10^{-1} and 1 µm and that corresponding to pores with radii in the interval between 1×10^{2} and 1×10^{3} µm are emphasized. The maximum intrusion percentages are 5.5% and 0.8%, respectively. No other peaks are observable at this temperature. Finally, at 1300 °C a maximum intrusion percentage of approximately 8.5%, which corresponds to pore radii between 1×10^{-1} and 1 µm, can be deduced. The pores with a radius in the interval between 1×10^{2} and 1×10^{3} µm have perceived a lower percentage of intrusion compared to the sample fired at 1200 °C (approximately 0.4%). Thus, the maximum percentage of intrusion increases with the firing temperature, mainly taking place in the pores with a radius between 1×10^{-1} and 1 µm. On the other hand, Table 4 shows the average of the pore radius values, expressed in microns, in every sample along with the mode and the total porosity expressed as a percentage. A decrease in the three parameters with the increase in the firing temperature is observed.

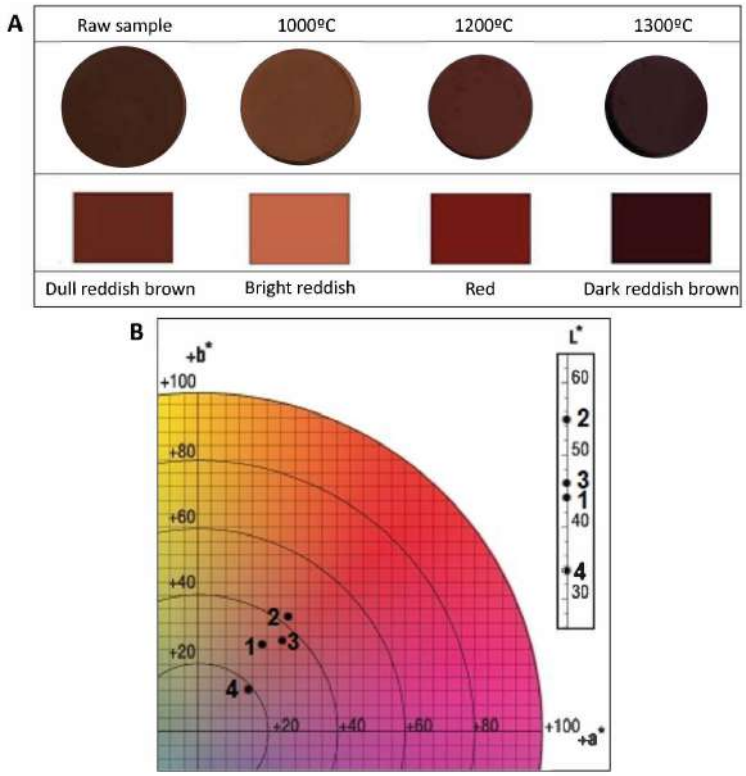

Figure 10. (**A**) Munsell scale values for the study specimens. (**B**) Plot of the data obtained in the CIE L*a*b* color space. Numbers 1, 2, 3 and 4 correspond, respectively, to the raw specimens and those fired at 1000, 1200 and 1300 °C.

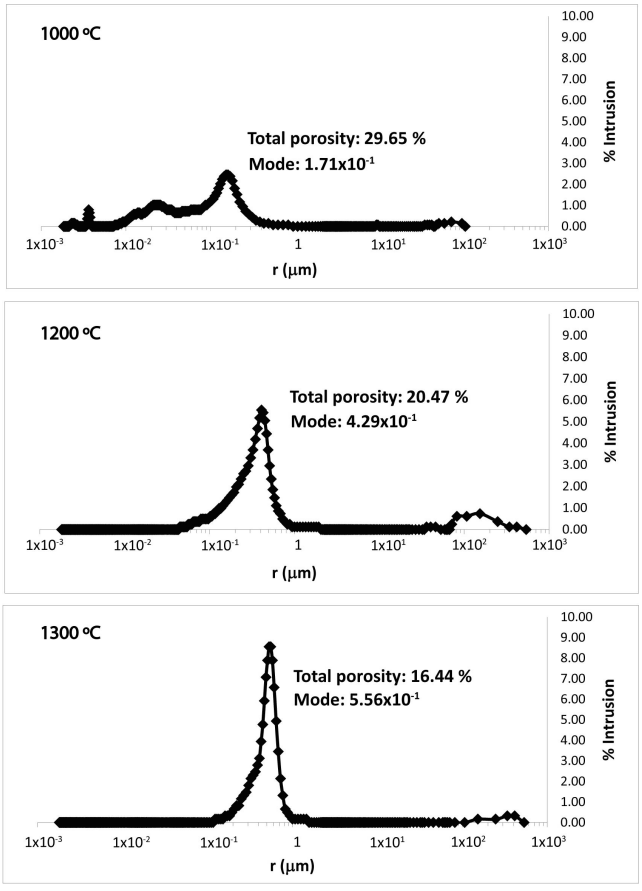

Figure 11. Pore volume distribution curves in samples fired at the different temperatures.

Table 4. Means and modes of the pore radii of the samples fired at the different temperatures expressed in μm as well as their total porosity, expressed in percentage.

T (°C)	Average (μm)	Mode (μm)	Total Porosity (%)
1000	4.90×10^{-2}	2.96	29.65
1200	3.21×10^{-2}	2.91×10^{-1}	20.47
1300	2.12×10^{-2}	5.35×10^{-2}	16.44

With regard to the point load test (PLT), no measurements could be obtained from the sample fired at 1000 °C, since the prisms obtained from the original cylinder broke up before the measuring device could register the point load necessary for the prism to break. The point load data recorded at the moment of failure for the prisms obtained from samples fired at 1200 °C and 1300 °C are shown in Figure 12. Figure 12 shows the percentage of broken prisms at every moment when a breakage occurred. Once the values considered anomalous obtained from the point load test have been disregarded, two trend lines of similar slopes are observed, one for every firing temperature. It can be stated that, in general, a greater point load has been necessary to produce the breakage of the prisms of the sample fired at a higher temperature. Once the maximum and minimum values of the series of measurements taken on the studied prisms have been disregarded, the average point load index I_{s50} is calculated for the specimens fired at 1200 and 1300 °C (Figure 12), with the point load index being higher for the sample fired at the highest temperature.

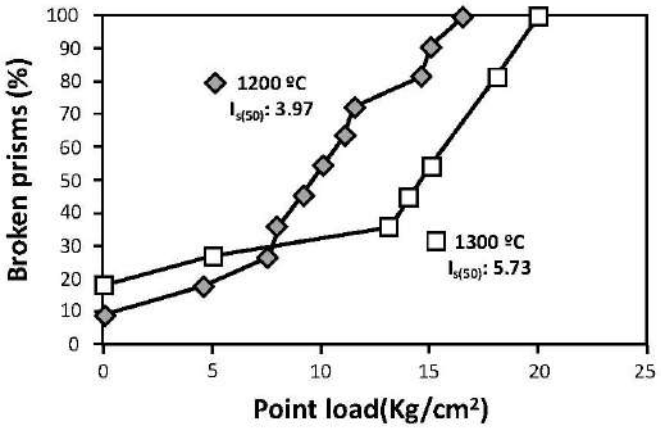

Figure 12. Percentage of broken prisms with the application of a certain point load.

5. Discussion

5.1. Origin of the Bauxite

From a geological point of view, the study of bauxites can be of interest since they can be used as palaeoclimatic indicators but also as raw material to extract alumina by means of the Bayer process. This lies in the fact that bauxite genesis requires very specific conditions, such as a tropical to humid subtropical climate, with rainfall of 1200 cm/year and temperatures of 22 °C [27]. Nowadays, the favorable areas for bauxitization are in latitudes between 30° N and 30° S [28]. However, as mentioned above, it is crucial to decipher several important issues such as the autochtonous/allochtonous nature of the deposits along with the possible superposition of different processes during bauxitization.

The idiomorphic to subidiomorphic character of the observed platy kaolinite crystals, together with the presence of book-type aggregates, too fragile to withstand long transport, would indicate an in situ formation [29,30]. Boehmite is also believed to have formed in situ, simultaneously with kaolinite or immediately afterwards, as evidenced by its presence as cement of the latter or between the layers of book-type aggregates. The

textural characteristics of the Fe oxides indicate a similar origin, as has been described in kaolin deposits [31]. The detected traces of other phases, such as rutile, anatase, quartz or micaceous phases, would have a detrital character and would be remains of the parent rock.

The in situ formation of the bauxitic phases took place both in the matrix of the parent rock and in cavities within it, as evidenced by FESEM observations, a feature that has also been described in the karst bauxites studied by [4,32]. The formation of kaolinite is linked to intense chemical weathering processes involving the dissolution of silicate phases such as quartz, feldspar and plagioclase, favoring the recrystallization of phases rich in relatively immobile cations (Al, Si, Fe), such as kaolinite, Al hydroxides and iron oxyhydroxides, and the leaching of mobile elements (K, Na, Ca) [33]. These authors also indicate that the presence of kaolinite, Al hydroxides and Fe oxyhydroxides, without the presence of quartz or feldspar, suggests a dissolution/crystallization development with a high fluid/rock ratio. Thus, they would have formed both from the dissolution of pre-existing phases bearing these elements and from direct precipitation from Al- and Si-rich fluids in void spaces, probably suggesting more than a single bauxitization episode. This does not necessarily imply strictly discrete bauxitization events, but rather suggests a complex, multistage or evolving bauxitization process characterized by successive changes in the physicochemical conditions.

The textural characteristics of the pisolithic particles seem to agree with the existence of several episodes during bauxitization. The presence of ooids and other particles in the core of some pisoids indicates the existence of several episodes of pisolith formation [34]. On the other hand, the variation in the proportions of the different phases that make up the concentric layers frequently observed in the pisoliths would indicate changes in the physical–chemical conditions during their formation. According to [1], for the formation of ooids and pisoids, the material has to be permanently saturated in water. The elongated morphologies observed in some of them could be related to this, indicating that during their formation they would be in a semi-plastic state. The adaptation of the concentric layers to particles or accumulations of certain phases, enveloping them, could also be related to the fact that probably, at the time of the formation of the pisoliths, they presented a semi-plastic state due to the water saturation of the environment. These facts indicate that the formation of the pisolithic particles took place, at least mostly, in situ, and therefore the bauxite under study can be considered autochtonous. The textural similarities of the matrix with the core of the pisoliths or the entire particle, in the case of massive ones, and, in general, with the mineral phases present in said particles also point to an in situ origin.

However, there is evidence that the pisolitic particles have also undergone a certain transport, as attested by the fractures observed in some of them, filled with the same phases of the matrix, and the existence of pisolith fragments in the matrix and in the core of several pisoids and ooids. Taking into consideration that the deposit would have been formed in several episodes or stages, it is possible that a certain reworking of the pisoliths occurred between the different episodes, which has been recorded in the aforementioned characteristics. However, this transport would not have been very intense given that unfractured pisoliths, without evidence of transport, are more abundant.

The formation of the bauxite under study, therefore, would indicate warm and humid climatic conditions in the study area during its formation. Regional paleoclimatic reconstructions indicate that during the Cretaceous, the circum-Mediterranean region experienced predominantly subtropical to tropical climatic conditions, favoring deep lateritic weathering and widespread bauxitization in combination with active tectonics linked to the closure of the Tethys Ocean [1,29,35]. This regional framework supports our interpretation of a tropical monsoon-type climate for the formation of the studied Lower Cretaceous deposit. These conditions would be similar to those prevailing during the formation of

other bauxite deposits in the NE of the Iberian Peninsula, such as those of Fuentespalda (Teruel), from the Lower Cretaceous, characterized by [4,32]. The studied outcrop between the Jurassic and Cretaceous and the Santonian/Campanian transit, would be located at a latitude close to the equator, approximately between latitude 10° N and 5° N [36]. Therefore, from the top of the Jurassic dolomites, which constitute the base of the outcrop, to the Santonian sands, to the top, the area is at a paleolatitude favorable for the formation of bauxites. According to the [37] classification of climates, in relation to the paleolatitude of the deposit at the time of its formation, the climate prevailing would be a tropical monsoon climate, so there would be favorable climatic conditions for the formation of bauxite.

5.2. Mineral and Textural Transformations During the Ceramic Process

In general, the increase in firing temperature implies a textural homogenization, with the appearance of diffuse reaction edges in the fragments of the original rocks and quartz, and evidence of fusion and recrystallization of a vitreous phase from 1200 °C (Figure 9). The firing process also involves the destabilization of some phases and the neoformations of others. As deduced from XRD, clays, boehmite and goethite disappear at 1000 °C, whereas hematite, quartz and, especially, mullite, along with minor amounts of corundum, ilmenite, and cristobalite, are neoformed.

With regard to clays (kaolinite and illite), at 500–550 °C the dehydroxylation of both phases takes place and, in the case of kaolinite, the formation of metakaolinite or pre-mullite occurs [15,38]. At about 950 °C, metakaolinite can be transformed into γ-alumina leading to the release of silica, which would favor the neoformation of cristobalite and quartz [39,40], as the XRD results evidenced. The destabilization of illite would also lead to the formation of amorphous silica from 925 to 1050 °C [41], from which quartz and cristobalite can crystallize, in agreement with the XRD data. FESEM observations revealed that typical morphologies of kaolinite and illite are still visible at 1000 °C (Figure 8B,D), but they show mullite compositions, which indicate that their destabilization and related release of silica also lead to the solid-state transformation of these phases into mullite.

Both quartz and amorphous silica present small oscillations in the firing systems, which would indicate that there is a solubilization–precipitation process between SiO_2 and Al_2O_3 [42,43]. Despite these oscillations, the trend is towards the destabilization of quartz with increasing temperature, as the XRD results evidenced, being almost absent at 1200 and 1300 °C compared to 1000 °C. This is also evidenced by FESEM observations, which showed the presence of a Si-rich vitreous or molten-looking phase surrounding the few quartz grains exhibiting reaction edges, as observed in the sample fired at 1200 °C (Figure 9B,C).

The XRD data indicate that boehmite and goethite are also unstable and have completely disappeared due to the dehydration processes at 1000 °C. Boehmite transforms into γ-alumina around 500 °C [15,44–46], detected by XRD, whereas goethite transforms into hematite between 500 and 600 °C [15,47,48]. On the other hand, FESEM analysis has demonstrated the existence at 1000 °C of solid solutions between Ti oxides and ilmenite, as evidenced by the observation of compositional zoning between these phases. Solid solutions between Fe and Ti oxides have also been described in refractory materials as a consequence of the firing process (e.g., [15] and references therein). The XRD results also show that, despite the neoformation of hematite at relatively low temperatures, it is partially destabilized at 1200 and 1300 °C. The analysis of hematite crystals shows aluminum compositions, indicative of recrystallization at these temperatures.

Corundum (α-alumina) neoformation, detected by XRD, would be justified by the existence of a solid solution between hematite and Al_2O_3 between 1000 and 1300 °C [49], as well as by the dehydration of boehmite which, as mentioned, transforms into γ-alumina

around 500 °C, which could suggest that the increase in temperature, in this case, up to 1000 °C, results in the formation of corundum, the most stable phase of alumina [45,50].

However, the most notable mineralogical change during firing is the formation of mullite, to a greater extent at higher temperatures (1200–1300 °C). As already mentioned, its formation is triggered by the thermal decomposition of kaolinite and illite. FESEM observations indicate that at higher firing temperatures the mullite crystals are larger (Figure 9E,F). On the other hand, EDS analyses have shown that at higher firing temperatures (1200 and 1300 °C) the mullite composition is closer to the empirical formula, with a lower Si/Al ratio. The observation of mullite crystals immersed in a vitreous matrix (Figure 9B,F) suggests that this mineral phase crystallized from molten material.

5.3. Mineral and Textural Transformations and Physical Properties of Calcined Ceramics

The physical properties of fired products are related to the mineralogical and textural changes that occur during firing. Density increases with firing temperature, showing a more pronounced increase between 1000 and 1200 °C than between 1200 and 1300 °C, which can be related to the formation of the vitreous phase that subsequently gives rise to mullite [51]. A similar behavior is observed in linear shrinkage, with a greater increase in this parameter between 1000 and 1200 °C, which would be related to the dehydroxylation of phyllosilicates, which starts from around 450 °C, although preserving their morphologies at 1000 °C [52], and the subsequent formation of mullite. On the contrary, there is no clear trend with regard to weight loss, which represents a value of approximately 12% in global terms. Presumably, it is related to the loss of H_2O and OH groups. The fact that the firing temperature barely influences this parameter suggests that there is no loss of other material. Regarding color, at 1000 °C a change from brown to a reddish hue is observed, coinciding with the highest hematite contents deduced from XRD. The change towards darker and eventually less red tones at higher temperatures is related to a decrease in hematite content and the extensive formation of mullite that represents approximately 80% of the samples fired at the highest temperatures.

The destabilization of kaolinite with the increase in firing temperature involves the formation of a vitreous phase and subsequent crystallization of mullite [53,54]. This fact would explain the decrease in porosity as obtained by the porosimetric analysis, since the vitreous phase and mullite would fill the pores of the material.

Regarding the results of the point load test, two trend lines of similar slopes were identified once the anomalous values, corresponding to defects in the prisms, were neglected (Figure 12). As quoted before, the test could only be carried out successfully on specimens fired at 1200 and 1300 °C. The substantial difference between the aforementioned samples and the sample fired at 1000 °C is the mullite content, varying from approximately 30% at 1000 °C to values around 85% at 1200 and 1300 °C. The differences in the results of the point load test in the latter could correspond to the greater development of the mullite crystals, as has been observed by means of FESEM observations. Therefore, at a higher firing temperature, a greater resistance of the fired materials is observed, which is related to a higher mullite content and a larger size of its crystals.

In general, therefore, it can be stated that, in terms of the mineralogical and textural changes and the physical properties and their variation with the firing temperature, there are notable changes between the specimens fired at 1000 °C but there are no major differences between the specimens fired at 1200 and 1300 °C, as density, shrinkage, color and porosity do not show significant variation between these two temperatures, whereas the mechanical behavior is enhanced at the highest temperature with greater point load resistance observed in the specimens fired at 1300 °C (~44% higher).

6. Conclusions

Regarding the genetic aspects of the deposit, kaolinite, boehmite and Fe oxides are authigenic phases, formed in situ during the bauxitization process, and the abundant pisoliths also formed in situ. The remaining identified phases, which occur as traces, are relics of the parent rock. Bauxitization took place through dissolution/crystallization mechanisms with a high fluid/rock ratio, together with direct precipitation of bauxitic phases from Al- and Si-rich fluids in void spaces. The formation of the bauxite indicates warm and humid climatic conditions, such as a tropical monsoon climate, which favored intense chemical weathering. The deposit would have formed in several episodes, with evidence of some reworking of the pisoliths between different stages.

With respect to the ceramic behavior and technological performance, increasing the firing temperature produces textural homogenization and the disappearance of clays, boehmite and goethite in the manufactured ceramics at 1000 °C, whereas hematite, quartz and, especially, mullite, together with minor amounts of corundum, ilmenite, and cristobalite, are neoformed. The destabilization of kaolinite and illite leads to solid-state transformation of these phases into mullite at 1000 °C, whereas at higher temperatures mullite crystallizes from molten material, forming larger crystals with compositions closer to the empirical mullite formula.

The physical properties of fired products are directly related to these mineralogical and textural changes. Density and linear shrinkage increase non-linearly with firing temperature, with the greatest increase between 1000 and 1200 °C, related to the formation of a vitreous phase and the dihydroxylation of phyllosilicates, respectively. Color changes are controlled by hematite content, whereas porosity decreases due to pore filling by the vitreous phase and the subsequent mullite crystallization.

No major differences are observed between specimens fired at 1200 and 1300 °C, except for the higher point load resistance at 1300 °C, which is related to the higher mullite content and larger crystal size. Therefore, bauxite shows potential interest for ceramic manufacturing, particularly due to the mechanical strength achieved in fired products.

Author Contributions: Conceptualization, A.Y.; methodology, A.Y. and E.L.; investigation, A.Y., B.B. and E.L.; resources, B.B. and A.Y.; writing—original draft preparation, A.Y.; writing—review and editing, B.B. and E.L.; supervision, B.B.; project administration, B.B.; funding acquisition, B.B. All authors have read and agreed to the published version of the manuscript.

Funding: The work was supported by the Spanish Ministry of Science, Innovation and Universities [grant number PID2021-123127OB-I00]. This publication is part of the grant JDC2022-048348-I funded by the MCIN/AEI/10.13039/501100011033 and by the European Union "NextGenerationEU"/PRTR.

Data Availability Statement: The original contributions presented in this study are included in the article. Further inquiries can be directed to the corresponding author.

Acknowledgments: The authors would like to acknowledge the use of Servicio General de Apoyo a la Investigación-SAI, Universidad de Zaragoza. The authors would also like to thank the reviewers and editor, whose comments and suggestions helped to improve the manuscript.

Conflicts of Interest: The authors declare no conflicts of interest.

References

1. Bardossy, G. *Karst Bauxites: Bauxite Deposits on Carbonate Rocks*; Elsevier: Amsterdam, The Netherlands, 1982; pp. 1–441.
2. Bardossy, G.; Combes, P.J. Karst bauxites: Interfingering of deposition and palaeoweathering. In *Palaeoweathering, Palaeosurfaces and Related Continental Deposits*; John Wiley & Sons: Hoboken, NJ, USA, 1999; Volume 27, pp. 189–206. [CrossRef]
3. Horbe, A.M.C. Oxygen and hydrogen isotopes in pedogenic minerals—Implications for paleoclimate evolution in Amazonia during the Cenozoic. *Geoderma* **2011**, *163*, 178–184. [CrossRef]

4. Yuste, A.; Bauluz, B.; Mayayo, M.J. Genesis and mineral transformations in Lower Cretaceous karst bauxites (NE Spain): Climatic influence and superimposed processes. *Geol. J.* **2015**, *50*, 839–857. [CrossRef]
5. Perkovic, I.; Blanka Cvetko TeŠovic, B.C.; MartinuŠ, M.; Vlahovic, I.; Razum, I.; Škapin, S.D.; Darko MateŠic, D.; Mihovilovic, M.; He, T.; Newton, R.J.; et al. Genesis of the Rovinj-1 bauxite deposit (Istria, Croatia): Record of palaeoclimatic trends and palaeoenvironmental changes during the latest Jurassic of the Adriatic Carbonate Platform. *Ore Geol. Rev.* **2024**, *173*, 106236. [CrossRef]
6. Mameli, P.; Mongelli, G.; Oggiano, G.; Dinelli, E. Geological, geochemical and mineralogical features of some bauxite deposits from Nurra (Western Sardinia, Italy): Insights on conditions of formation and parental affinity. *Int. J. Earth Sci.* **2007**, *96*, 887–902. [CrossRef]
7. Sinisi, R. Mineralogical and geochemical features of Cretaceous bauxite from San Giovanni Rotondo (Apulia, Southern Italy): A provenance tool. *Minerals* **2018**, *8*, 567. [CrossRef]
8. Traoré, S.; Diarra, A.; Kourouma, O.; Traoré, D.L. Survey of Bauxite Resources, Alumina Industry and the Prospects of the Production of Geopolymer Composites from the Resulting by-product. In *Geopolymers and Other Geosynthetics*; Alshaaer, M., Jeon, H.Y., Eds.; IntechOpen: London, UK, 2019. [CrossRef]
9. Zainudeen, N.M.; Mohammed, L.; Nyamful, A.; Adotey, D.; Osae, S.K. A comparative review of the mineralogical and chemical composition of African major bauxite deposits. *Heliyon* **2023**, *9*, e19070. [CrossRef]
10. Martínez, A.; Garcia-Valles, M.; Alfonso, P. Viability of Bauxite Deposits from Catalonia (Spain) for Ceramic Applications. *Minerals* **2023**, *13*, 1294. [CrossRef]
11. Zheng, S.; Zhou, X.; Xing, W.; Zhao, P. Analysis on the evolution characteristics of kaolin international trade pattern based on complex networks. *Resour. Policy* **2022**, *77*, 102783. [CrossRef]
12. Altun, I.A. Effect of temperature on the mechanical properties of self-flowing low cement refractory concrete. *Cem. Concr. Res.* **2001**, *31*, 1233–1237. [CrossRef]
13. Briggs, J. The refractories industry-A review. *Mater. Technol.* **2005**, *20*, 225–232. [CrossRef]
14. Jordán, M.M.; Meseguer, S.; Pardo, F.; Montero, M.A. High-temperature mineral formation after firing clay materials associated with mined coal in teruel (Spain). *Appl. Sci.* **2020**, *10*, 3114. [CrossRef]
15. Laita, E.; Bauluz, B.; Mayayo, M.J.; Yuste, A. Mineral and textural transformations in mixtures of Al-rich and Al–K-rich clays with firing: Refractory potential of the fired products. *Ceram. Int.* **2021**, *47*, 14527–14539. [CrossRef]
16. Dong, Y.; Feng, X.; Feng, X.; Ding, Y.; Liu, X.; Meng, G. Preparation of low-cost mullite ceramics from natural bauxite and industrial waste fly ash. *J. Alloys Compd.* **2008**, *460*, 599–606. [CrossRef]
17. Khalil, N.M.; Algamal, Y.; Salee, Q.M. Exploitation of petroleum waste sludge with local bauxite raw material for producing high-quality refractory ceramics. *Ceram. Int.* **2018**, *44*, 18516–18527. [CrossRef]
18. Maggetti, M. Phase analysis and its significance for technology and origin. In *Archaeological Ceramics Smithsonian*; Olin, J.S., Ed.; Institution Press: Boston, MA, USA, 1982; pp. 121–133.
19. Molina, J.M.; Ruiz-Ortiz, P.A.; Vera, J.A.; Calonge, A. Bauxitas kársticas de la sierra de Boada (Sierras Marginales surpirenaicas, Alós de Balaguer, Lleida). *Geogaceta* **1994**, *16*, 148–150.
20. Teixell, A. The Ansó transect of the southern Pyrenees: Basament and cover thrust geometries. *J. Geol. Soc.* **1996**, *153*, 301–310. [CrossRef]
21. Sauila i Briansó, E.; Samsó, J.; Escuer, J.; Casanovas, J. *Mapa Geológico de España 328*; IGME: Madrid, Spain, 2000; pp. 1–99.
22. Pocoví, A. Estudio geológico de las Sierras Marginales Catalanas (Prepirineo de Lérida). *Acta Geol. Hisp.* **1978**, *XIII*, 73–79.
23. Combes, P.J. Recherches Sur La Gènese des Bauxites Dans Le Nord-Est de L'Espagne, Le Languedoc et L'Ariège (France). Ph.D. Thesis, Université de Montpellier, Montpellier, France, 1969.
24. Martín, J.D. A software package for powder X-ray diffraction analysis. In *Qualitative, Quantitative and Microtexture*; XPowder: Granada, Spain, 2017; 121p. Available online: https://www.xpowder.com/ (accessed on 10 April 2025).
25. Smith, D.K.; Johnson, G.G., Jr. Digitized database quantification, DDBQ, analysis of complex mixtures using fully digitized patterns. *Adv. X-Ray Anal.* **2000**, *42*, 276–286.
26. Biscaye, P.E. Mineralogy and sedimentation of recent deep-sea clay in the Atlantic Ocean and adjacent seas and ocean. *Geol. Soc. Am. Bull.* **1965**, *76*, 803–832. [CrossRef]
27. Bardossy, G.; Aleva, G.J.J. *Lateritic Bauxites*; Elsevier: Amsterdam, The Netherlands, 1990; pp. 1–624.
28. Bardossy, G.; Dercourt, J. Les gisements de bauxites téthysiens (Méditerranée, Proche et Moyen Orient); cadre paléogéographique et contrôles génétiques. *Bull. De La Soc. Géol. De Fr.* **1990**, *8*, 869–888. [CrossRef]

29. Do Campo, M.; Bauluz, B.; Del Papa, C.; White, T.; Yuste, A.; Mayayo, M.J. Evidence of cyclic climatic changes recorded in clay mineral assemblages from a continental Paleocene-Eocene sequence, northwestern Argentina. *Sediment. Geol.* **2018**, *368*, 44–57. [CrossRef]
30. Laita, E.; Bauluz, B.; Aurell, M.; Bádenas, B.; Yuste, A. Weathering events recorded in uppermost Hauterivian–lower Barremian clay-dominated continental successions from the NW Iberian Range: Climatic vs. tectonic controls. *J. Iber. Geol.* **2022**, *48*, 45–63. [CrossRef]
31. Sayed, E.; Youssef, A.A. Sedimentological studies on the central Wadi Kalabsha kaolin deposits, Southwest of Aswan, Egypt. *J. Mineral. Petrol. Econ. Geol.* **1996**, *91*, 353–363. [CrossRef]
32. Yuste, B.; Bauluz, B.; Mayayo, M.J. Origin and geochemical evolution from ferrallitized clays to karst bauxite: An example from the lower cretaceous of NE Spain. *Ore Geol. Rev.* **2017**, *84*, 67–79. [CrossRef]
33. Bauluz, B.; Yuste, A.; Mayayo, M.J.; Canudo, J.I. Early kaolinization of detrital Weald facies in the Galve Sub-basin (Central Iberian Chain, north-East Spain) and its relationship to palaeoclimate. *Cretac. Res.* **2014**, *50*, 214–227. [CrossRef]
34. Mücke, A.; Badejoko, A.; Akande, S.O. Petrographic-microchemical studies and origin of the Agbaja Phanerozoic Ironstone Formation, Nupe Basin, Nigeria: A product of a ferruginized ooidal kaolin precursor not identical to the Minette-type. *Miner. Depos.* **1999**, *34*, 284–296. [CrossRef]
35. Mondillo, N.; Di Nuzzo, M.; Kalaitzidis, S.; Boni, M.; Santoro, L.; Balassone, G. Petrographic and geochemical features of the B3 bauxite horizon (Cenomanian-Turonian) in the Parnassos-Ghiona area: A contribution towards the genesis of the Greek bauxites. *Ore Geol. Rev.* **2022**, *143*, 104759. [CrossRef]
36. Dercourt, J.; Zonenshain, L.P.; Ricou, L.E.; Kazmin, V.G.; Le Pichon, X.; Knipper, A.L.L.; Grandjacquet, C.; Sbortshikov, I.M.; Geyssant, J.; Lepvrier, C.; et al. Geological evolution of the Tethys belt from the Atlantic to the Pamirs since the Lias. *Tectonophysics* **1986**, *123*, 241–315. [CrossRef]
37. Köppen, W. Klassifikation der Klima nach Temperatur, Niederschlag und Jahreslauf. *Petermans* **1918**, *64*, 193–203, 243–248.
38. Drits, V.; McCarty, D. The nature of structure-bonded H2O in illite and leucophyllite from dehydration and dehydroxylation experiments. *Clays Clays Miner.* **2007**, *55*, 45–48. [CrossRef]
39. Brindley, G.W.; Nakahira, M. The Kaolinite—Mullite reaction series. *J. Am. Ceram. Soc.* **1959**, *43*, 314–324. [CrossRef]
40. Duval, D.J.; Risbud, S.H.; Shackelford, J.F. Mullite. In *Ceramic and Glass Materials, Structure, Properties and Processing*; Shackelford, J.F., Doremus, R.H., Eds.; Springer: New York, USA, 2008; pp. 27–39. [CrossRef]
41. Ondro, T.; Al-Shantir, O.; Csáki, Š.; Lukác, F.; Trník, A. Kinetic analysis of sinter-crystallization of mullite and cristobalite from kaolinite. *Thermochim. Acta* **2019**, *678*, 178312. [CrossRef]
42. Srodon, J. Identification and quantitative analysis of clay minerals. Handbook of clay Science. In *Developments in Clay Science*; Bergaya, F., Theng, B.K.G., Lagaly, G.M., Eds.; Elsevier: Amsterdam, The Netherlands, 2006; pp. 765–787. [CrossRef]
43. Zevin, L.; Viaene, W. Impact of clay particle orientation on quantitative clay diffractometry. *Clay Miner.* **1990**, *25*, 401–418. [CrossRef]
44. Panias, D.; Krestou, A. Effect of synthesis parameters on precipitation of nanocrystalline boehmite from aluminate solutions. *Powder Technol.* **2007**, *175*, 163–173. [CrossRef]
45. Jbara, A.S.; Othaman, Z.; Ati, A.A.; Saeed, M.A. Characterization of γ-Al2O3 nanopowders synthesized by Co-precipitation method. *Mater. Chem. Phys.* **2017**, *188*, 24–29. [CrossRef]
46. Dong, Y.; Zhang, M.; Xie, C. Effect of reaction conditions on agglomeration of aluminium hydroxide in the recovery of waste aluminium-catalyst. *Sep. Purif. Technol.* **2020**, *248*, 116978. [CrossRef]
47. Jang, K.; Nunna, V.R.M.; Hapugoda, S.; Nguyen, A.; Bruckard, W.J. Chemical and mineral transformations of a low grade goethite ore by dehydroxilation, reduction roasting and magnetic separation. *Miner. Eng.* **2014**, *60*, 14–22. [CrossRef]
48. Sun, Y.; Zhu, X.; Han, Y.; Li, Y.; Gao, P. Iron recovery from refractory limonite ore using suspension magnetization roasting: A pilot-scale study. *J. Clean. Prod.* **2020**, *261*, 121221. [CrossRef]
49. Feenstra, A.; Sämann, S.; Wunder, B. An Experimental Study of Fe-Al Solubility in the System Corundum-Hematite up to 40 kbar and 1300 °C. *J. Petrol.* **2005**, *46*, 1881–1892. [CrossRef]
50. Cava, S.; Tebcherani, S.M.; Pianaro, S.A.; Paskocimas, C.A.; Longo, E.; Varela, J.A. Structural and spectroscopic analysis of γ-Al_2O_3 to α-Al_2O_3-$CoAl_2O_3$ phase transition. *Mater. Chem. Phys.* **2006**, *97*, 102–108. [CrossRef]
51. Andrews, A.; Adam, J.; Gawu, S.K.Y. Development of fireclay aluminosilicate refractory from lithomargic clay deposits. *Ceram. Int.* **2012**, *39*, 779–783. [CrossRef]
52. Guggenheim, S.; Chang, Y.H.; Koster van Groos, A.F. Muscovite dehydroxylation; high-temperature studies. *Am. Mineral.* **1987**, *72*, 537–550.

53. Chen, C.Y.; Lan, G.S.; Tuan, W.H. Microstructural evolution of mullite during the sintering of kaolin powder compacts. *Ceram. Int.* **2000**, *26*, 715–720. [CrossRef]
54. Meng, Y.; Gong, G.; Wei, D.; Xie, Y. In situ high temperature X-ray diffraction study on high strength aluminous porcelain insulator with the Al2O3-SiO2-K2O-Na2O system. *Appl. Clay Sci.* **2016**, *132*, 760–767. [CrossRef]